Vibrational resonance and ghost-vibrational resonance occurrence in Chua's circuit models with specific nonlinearities

B.I. Usama, Saverio Morfu, P. Marquie

Version of Record: https://www.sciencedirect.com/science/article/pii/S0960077921008699
Manuscript_533a8ae56bb4acb1ed3720c7a36c3c50

Vibrational resonance and ghost-vibrational resonance occurrence in Chua's circuit models with specific nonlinearities

B. I. Usama, S. Morfu[1], P. Marquie

ImViA EA 7535, Univ. Bourgogne Franche-Comté, F-21000 Dijon, France.

Abstract

This work numerically investigates the dynamics of a Chua's circuit model experiencing a truncated sinusoidal force and driven by an external perturbed excitation. We mainly study the impact of the system's nonlinearity on the occurrence of Vibrational Resonance (VR) and Ghost-Vibrational Resonance (GVR) phenomena. When a truncated sinusoidal nonlinearity is used, the system requires relatively smaller perturbation amplitude to attain its maximum response better than the one achieved with a sawtooth nonlinearity which requires a larger perturbation amplitude. Therefore, the system with a truncated sinusoidal nonlinearity outperforms the one with a sawtooth nonlinearity. Exciting the system with two low frequency inputs and an additive high frequency perturbation, we identify different ranges of the perturbation amplitude in which the occurrence of VR and GVR phenomena are maximized. We show that depending on the perturbation amplitude, the system can synchronize its response with the ghost frequency or one of the two input low frequencies.

Keywords: Nonlinear dynamics, Multistability, Vibrational resonance, Ghost-vibrational resonance.

1. Introduction

Due to its unpredictable nature and applications, nonlinearity has become a dominant property for exploration in all fields ranging from medical to cognitive and neurosciences. Biological models ruled by Hodgkin-Huxley or FitzHugh-Nagumo equations as well as electronic circuit models such as the famous Chua's circuit model, have revealed diverse fascinating nonlinear dynamical properties for decades. Among the trending and most studied dynamical effects in nonlinear systems are undoubtedly Stochastic Resonance (SR) and Vibrational Resonance (VR). SR effect [1] is a resonance induced phenomenon where a weak signal interacts in a nonlinear systems with a random noise perturbation to produce a better signal response at the system output. By contrast, for VR effect [2], the system's response to an input low frequency signal is improved by adding an appropriate amount of a high frequency perturbation instead of noise. VR and SR effects have attracted considerable attention due to their outstanding applications and were studied both theoretically and experimentally in many systems [3, 4, 5, 6, 7, 8, 9, 10, 11, 12, 13, 14] and in different contexts [15, 16, 17, 18, 19].

Especially, the observation of VR and SR phenomena in electronic circuits have led to many applications ranging from signal to image processing. More specifically, SR has revealed the possibility to enhance visual perception [20, 21]. Recently, it has been shown that VR can enhance the perception of subthreshold noisy images [22]. VR has also revealed potential applications in image processing which are still under investigation [23]. Because of these promising applications, properties of VR and SR are widely under investigation.

[1]Corresponding author: smorfu@u-bourgogne.fr

October 5, 2021

More surprisingly, excitable nonlinear systems corrupted with an external input perturbation, can induce resonance in their output signal at a missing frequency lower than the input frequencies. Resonance induced at a missing low frequency due to a noise perturbation is called Ghost-Stochastic Resonance (GSR) [24, 25, 26, 27], whereas that alternatively induced by a high frequency perturbation is termed Ghost-Vibrational Resonance (GVR) [28, 29]. In this paper, we focus on VR and GVR occurrence and their properties in a modified Chua's circuit model experiencing a truncated sinusoidal nonlinearity.

On the other hand, the nature of the nonlinearity have significant impact on the dynamical response of nonlinear systems. For instance, a multistable nonlinearity has proven to have applications in image processing [30]. In particular, Chua's circuit model, which was first introduced to study chaotic behavior in electronic circuits, is based on a multistable nonlinearity [31]. This model was used to study many nonlinear properties and phenomena such as the existence of multi-scroll chaotic attractors [32, 33], bifurcation analysis [34, 35], SR [36], VR [28, 37] and GVR [28].

Recently, Chua's circuit model was used with a multistable sawtooth force as form of nonlinearity to study the occurrence of VR and GVR [28]. However, we must admit that the dynamics of Chua's circuit model in the context of nonlinear resonances was not explored with a truncated sinusoidal force, which is also multistable. Indeed, nonlinear systems with the truncated sinusoidal force have revealed applications in image processing [30] and have also enabled information storage in memristors [38, 39, 40]. Owing to these promising applications, it is of crucial interest to characterize the impact of a truncated sinusoidal nonlinearity on VR and GVR occurrence. In this paper, we study how a truncated sinusoidal force affects the occurrence of VR and GVR in a modified Chua's circuit model. Moreover, we compare the dynamics of this model with our proposed nonlinearity and the one studied by K. Abirami *et al*, which considered nonlinearity consisting of a periodic sawtooth function [28].

The subsequent sections of this paper are arranged in the following order. Firstly, the system under consideration is described in Section 2 with its setup and the numerical procedure used throughout the paper. Next, the analyses of the VR and GVR are presented in Sections 3 and 4 respectively. Lastly, section 5 is devoted to the conclusion and outlooks of our studies.

2. Description of the system

Chua's circuit was first invented in 1983 by Leon O. Chua to study the existence of double-scroll chaotic attractors occuring in the system with a piece-wise linear function [31]. These attractors were numerically confirmed in 1984 by Matsumotu [41] and the chaotic behavior of the circuit was experimentally shown one year later [42]. The modification of the initial nonlinearity of the system has also attracted attention, which initially presented two attractors since it has allowed to generate multi-scroll attractors by increasing the number of equilibrium points [33]. In this paper, we also focus on the impact of the nonlinearity and its multistable properties on the dynamics of the following modified Chua's circuit model:

$$\begin{aligned} \frac{dx}{dt} &= \alpha y + \frac{d\Phi_n(x,\alpha)}{dx} + e_p(t) \\ \frac{dy}{dt} &= x - y + z \\ \frac{dz}{dt} &= -\beta y. \end{aligned} \tag{1}$$

In this paper, the system is set such that it does not exhibit chaos in absence of driving and it presents equilibrium points defined by the potential $\Phi_n(x,\alpha)$. This three dimensional system describes the evolution of three variables x, y and z, when it is driven by an input perturbed excitation $e_p(t)$. The term $\Phi_n(x,\alpha)$ is a nonlinear potential which provides the multistability and whose derivative

will refer to a nonlinearity of order n in the whole article. Moreover, α is a constant parameter which also adjusts the height of the potential barrier. The corresponding nonlinear force $F_n(x,\alpha)$ is derived from the potential $\Phi_n(x,\alpha)$ by the relation

$$F_n(x,\alpha) = -\frac{d\Phi_n(x,\alpha)}{dx}. \tag{2}$$

2.1. The nonlinear force $F_n(x,\alpha)$

The most crucial part of the Chua's circuit model defined by the set of eqs. (1) is the nonlinear force $F_n(x,\alpha)$ due to its significant impact on the dynamical response of the system. Indeed, variety of dynamical behaviors were studied while considering different nonlinear forces or nonlinearities $F_n(x,\alpha)$ such as: a sigmoid force [43], a piecewise linear force [44], a discontinuous force [45], a saturated force [46] and a sawtooth force [33, 36, 28] among others.

A recent study by K. Abirami *et al* reported the role of a sawtooth type nonlinearity on VR and GVR occurrence in a modified Chua's circuit model [28]. This sawtooth force is redefined here with our own notations for convenience and to allow direct comparison with the nonlinearity proposed in this paper. The sawtooth force of order n and parameter λ is then redefined by the following expression:

$$\begin{aligned} F_n(x,\alpha) = -\alpha\Bigg\{ \frac{A_0}{A}x + \left(\frac{(-1)^n+1}{2}\right) A_0\ \mathrm{sgn}(x) - \\ A_0 \sum_{j=0}^{n}\Bigg[\mathrm{sgn}\left(x + \left(2j - \left(\frac{(-1)^n-1}{2}\right)\right)A\right) + \\ \mathrm{sgn}\left(x - \left(2j - \left(\frac{(-1)^n-1}{2}\right)\right)A\right)\Bigg]\Bigg\}, \end{aligned} \tag{3}$$

where *sgn* is a sign function, n is the order of nonlinearity and the constant parameters α, A and A_0 adjust the potential barrier. The sawtooth force $F_n(x,\alpha)$ described by eq. (3) is presented in Fig. 1 with its corresponding potential $\Phi_n(x,\alpha)$ for two values of the nonlinearity order, namely $n=0$ and $n=1$.

The number of stable and unstable states of the potential is controlled by n. Indeed, for each value of n, we obtain $n+1$ unstable states and $n+2$ stable states, whose positions are given by

$$X^*_{h,n} = \frac{h}{4A} \quad ,$$

where h is an integer value in the interval $[-(n+1); n+1]$, while the second index n refers to the nonlinearity order. The parameter n categorizes these stability positions in two cases:

- if n is odd, the positions $X^*_{h,n} = \dfrac{h}{4A}$ correspond to stable states for even values of h and unstable states for odd values of h.
- if n is even, the positions $X^*_{h,n} = \dfrac{h}{4A}$ correspond to stable states for odd values of h and unstable states for even values of h.

Moreover, for all values of n, the potential starts at the left with a stable state at the position $X^*_{-(n+1),n} = -\dfrac{n+1}{4A}$ and ends at the right with a stable state at position $X^*_{(n+1),n} = \dfrac{n+1}{4A}$. The potential barrier height $\Delta\Phi$ associated to the sawtooth force is defined by $\Delta\Phi = \dfrac{\alpha A_0}{32A^3}$ and the spacing ΔX^* between any two consecutive stable or unstable

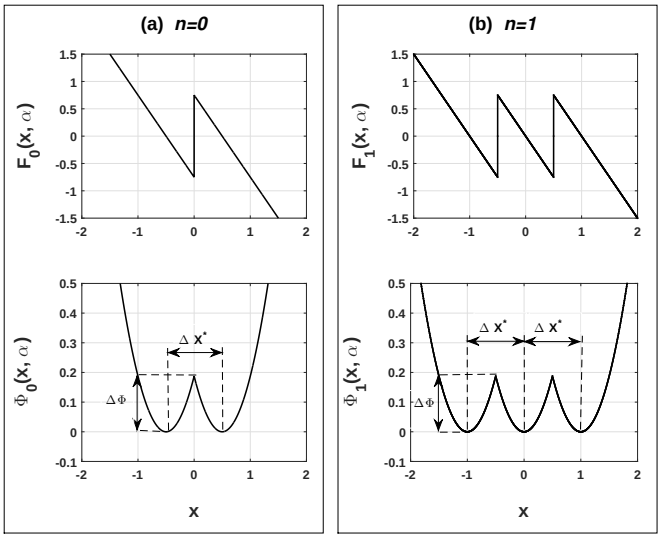

Figure 1: Sawtooth force $F_n(x,\alpha)$ and its corresponding potential $\Phi_n(x,\alpha)$ for two values of nonlinearity order n: (a) $n=0$, (b) $n=1$. Parameters: $\alpha=6$, $A=0.5$, $A_0=0.125$. ΔX^* represents the spacing between two consecutive stable or unstable states that is, the potential width and $\Delta\Phi$ is the potential barrier height.

states of the potential is given as $\Delta X^* = \dfrac{1}{2A}$.

In this paper, we introduce another multistable nonlinearity to investigate its impact on the dynamics of the modified Chua's circuit model, especially in the context of VR and GVR. More precisely, we propose a truncated sinusoidal force which is expressed as:

$$F_n(x,\alpha) = \begin{cases} -2\pi\alpha V_0 k^2[x + X^*_{(n+1),n}], \\ \qquad \text{for } x < X^*_{-(n+1),n} \\ -(-1)^n \alpha V_0 k[\sin(2\pi k x)], \\ \text{for } X^*_{-(n+1),n} \leq x \leq X^*_{(n+1),n} \\ -2\pi\alpha V_0 k^2[x + X^*_{-(n+1),n}], \\ \qquad \text{for } x > X^*_{(n+1),n} \ . \end{cases} \tag{4}$$

In eq. (4), as for the potential driven from the sawtooth force, $X^*_{-(n+1),n}$ and $X^*_{(n+1),n}$ correspond to the respective positions of the two ends of the potential associated to our truncated sinusoidal force. Moreover, the truncated sinusoidal force defined in eq. (4) is also multistable owing to its sinusoidal behavior. Note also that it is truncated because the force is replaced by the tangent of the sinusoidal function at both the two ends of the force as expressed in relation (4). Fig. 2 illustrates the form of the truncated sinusoidal force $F_n(x,\alpha)$ and its corresponding potential $\Phi_n(x,\alpha)$ for the orders of the nonlinearity $n = 0$ and $n = 1$. In the definition of the truncated sinusoidal force given by eq. (4), the parameter k accounts for the periodicity and width of the potential ΔX^*. Moreover, α and V_0 adjust the potential barrier height $\Delta\Phi$.

Similarly, n sets the number of stable and unstable states of the potential. Furthermore, this potential still exhibits $n+1$ unstable states and $n+2$ stable states located at positions

$$X^*_{h,n} = \frac{h}{2k} \ ,$$

where h is an integer in the range $[-(n+1);(n+1)]$ and the second index n refers to the nonlinearity order. The stability of each of these positions depends on the parity

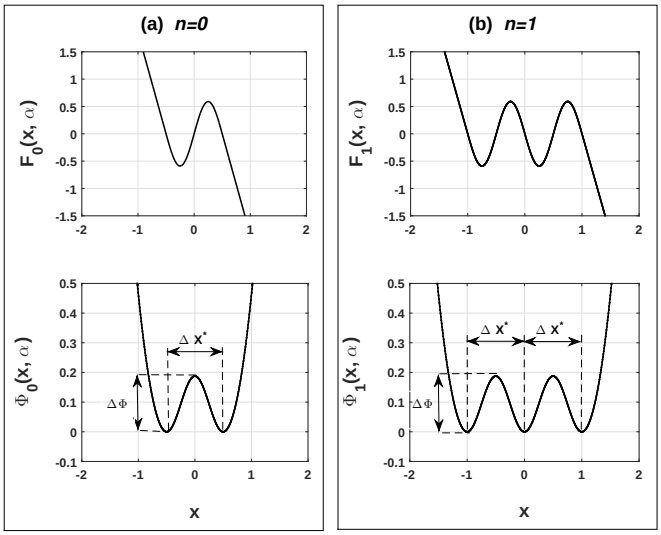

Figure 2: Truncated sinusoidal force $F_n(x,\alpha)$ and its corresponding potential $\Phi_n(x,\alpha)$ for two values of nonlinearity order n: (a) $n = 0$, (b) $n = 1$. Parameters: $\alpha = 6$, $V_0 = \dfrac{\pi}{32}$, $k = 1$. ΔX^* represents the spacing between two consecutive stable or unstable states and $\Delta\Phi$ is the potential barrier height.

of n:

- if n is odd, the positions $X^*_{h,n} = \dfrac{h}{2k}$ correspond to stable states for even values of h and unstable states for odd values of h.
- if n is even, the positions $X^*_{h,n} = \dfrac{h}{2k}$ correspond to stable states for odd values of h and unstable states for even values of h.

Lastly, whatever the value of n, the two ends of the potential correspond to stable states whose positions are given as $X^*_{-(n+1),n} = -\dfrac{(n+1)}{2k}$ and $X^*_{(n+1),n} = \dfrac{(n+1)}{2k}$. The barrier height of the potential driven from the truncated sinusoidal force, defined in eq. (4), is $\Delta\Phi = \dfrac{\alpha V_0}{\pi}$ and the spacing between any consecutive stable or unstable states of the truncated sinusoidal potential is given by $\Delta X^* = \dfrac{1}{k}$.

To compare the respective impact of the two nonlinearities defined by eqs. (3) and (4) on the system's response, it is necessary that the corresponding potentials share the same features in terms of barrier height $\Delta\Phi$ and width ΔX^*. This implies that, for our truncated sinusoidal force,

the parameter V_0 must be tuned to $V_0 = \frac{\pi A_0}{32A^3}$ while the periodicity k of the truncated sinusoidal potential must be adjusted to $k = 2A$.

In the study of K. Abirami *et al* [28], the parameters A_0 and A of their sawtooth force were adjusted to $A_0 = 0.125$ and $A = 0.5$. Consequently, throughout this paper, the parameters of our truncated sinusoidal nonlinearity are set to $V_0 = \frac{\pi}{32}$ and $k = 1$. With these parameters settings, both potentials of the two models share the same potential barrier height $\Delta\Phi$ and width ΔX^*, that is numerically $\Delta\Phi = \frac{\alpha}{32}$ and $\Delta X^* = 1$.

2.2. *Input perturbed excitation* $e_p(t)$

The system defined by eqs. (1) is driven by an input perturbed excitation $e_p(t)$ consisting of low frequency signal(s), corrupted by an additive high frequency perturbation, that is,

$$e_p(t) = e(t) + p(t). \tag{5}$$

Here, $e(t)$ refers to the input low frequency signal(s) defined as

$$e(t) = b\cos(\omega_1 t)\delta + b\Big[\cos(\omega_1 t) + \cos(\omega_2 t)\Big](1-\delta), \tag{6}$$

where the boolean variable δ allows to select the appropriate stimuli to investigate VR ($\delta = 1$) or GVR ($\delta = 0$). In eq. (6), the parameter b represents the low frequency amplitude whereas ω_1 and ω_2 are two close low angular frequencies whose difference will define the ghost angular frequency ω_0. Therefore, in the whole paper, we choose ω_1 and ω_2 so that they satisfy the classical setting to observe GVR, that is $\omega_1 = 2\omega_0$ and $\omega_2 = 3\omega_0$. Lastly, in the input perturbed excitation $e_p(t)$ defined by eq. (5), $p(t)$ stands for the high frequency perturbation which satisfies

$$p(t) = B\cos\Omega t. \tag{7}$$

In expression (7), B and Ω are the perturbation amplitude and its angular frequency respectively. Throughout this paper, we consider the high angular frequency to be much greater than the low angular frequencies namely, $\Omega \gg \omega_1$ and $\Omega \gg \omega_2$, which corresponds to the commonly used condition for achieving VR and GVR phenomena.

In absence of driving ($e_p(t) = 0$), according to the nullclines of the system (1) ($\frac{dx}{dt} = 0$, $\frac{dy}{dt} = 0$, $\frac{dz}{dt} = 0$), the equilibrium points are directly defined by the roots of the nonlinearity $F_n(x, \alpha)$. From a physical point of view, the system remains in its rest states near the stable states. The low frequency drivings $e(t)$, with weak amplitudes do not allow the crossing of the potential barrier inducing a response which is a slow amplitude oscillation near the rest state. Next, including the high frequency perturbation $p(t)$ involves the crossing of the potential barrier and then induces large excursions synchronized with the low frequencies.

2.3. *General numerical procedure*

To study the dynamics of the system described by the set of eq. (1), it is pertinent to first define the numerical procedure. Taking into account zero initial conditions for all variables, namely $x(0) = y(0) = z(0) = 0$, and by using the fourth order Runge-Kutta algorithm, we integrate the system of eq. (1) with each of the two types of nonlinearities defined by eqs. (3) and (4) respectively, and which is driven by the input excitation of eq. (5). Considering first the zero perturbation case, that is $B = 0$, we perform simulations during a temporal window T which corresponds to 1000 low frequency cycles and 2^{22} total number of samples. The corresponding integrating time step is therefore $dt = (\frac{1000}{2^{22}})\frac{2\pi}{\omega_i}$, with ω_i taken as $\omega_i = \omega_1$ for the study of VR ($\delta = 1$) and considered as $\omega_i = \omega_0$, ω_1 or ω_2 for the study of GVR ($\delta = 0$). When the perturbation amplitude B increases with step ΔB, last values of the system variables are considered as the initial conditions for the next simulation with amplitude $B + \Delta B$, that is $x(0) = x(T)$, $y(0) = y(T)$ and $z(0) = z(T)$. Lastly, the values of the output $x(t)$ corresponding to the last 500 driving cycles are considered for all computations whereas the first 500 cycles are discarded as transient.

3. Vibrational resonance occurrence

In order to study VR, the boolean variable δ is set to $\delta = 1$ in eq. (6). This reduces the input perturbed excitation $e_p(t)$ defined by eq. (5) to

$$e_p(t) = b\cos\omega_1 t + B\cos\Omega t. \tag{8}$$

In this section, we study how the multistable nonlinearities defined by eqs. (3) and (4) affect VR. Three different analyses are presented namely: temporal, frequency and phase portraits analyses. The constant parameters α and β are taken as $\alpha = 6$ and $\beta = 16$. Moreover, we set the amplitude of the low frequency to $b = 0.1$, the low angular frequency to $\omega_1 = 1$ and the perturbation angular frequency to $\Omega = 10\omega_1$.

3.1. Temporal analysis

In this subsection, we study how the temporal response $x(t)$ of the system experiencing truncated sinusoidal force behaves against the perturbation amplitude B.

The time series analysis is performed in such a way that, we increase the perturbation amplitude starting from $B = 0$ with the step $\Delta B = 0.01$ until $B = 1.5$, $B = 4.13$ and $B = 6.8$, to obtain the chronograms of Fig. 3(a), (b) and (c) respectively. The temporal series of Fig. 3 reveal that the low frequency signal is corrupted by the high frequency perturbation in all the three cases. For the smallest perturbation amplitude, that is $B = 1.5$ at Fig. 3(a), the low frequency contribution in the output signal is weak. However, for the intermediate perturbation amplitude $B = 4.13$ at Fig. 3(b), the low frequency component in the output signal is better revealed. The low frequency contribution in the output signal at Fig. 3(c) becomes less pronounced as the perturbation amplitude further increases to $B = 6.8$. This implies that when the perturbation amplitude B is optimally tuned to the intermediate value $B = 4.13$, a better enhancement of the system response to the low frequency excitation is achieved. This behavior signifies the occurrence of VR phenomenon in our system.

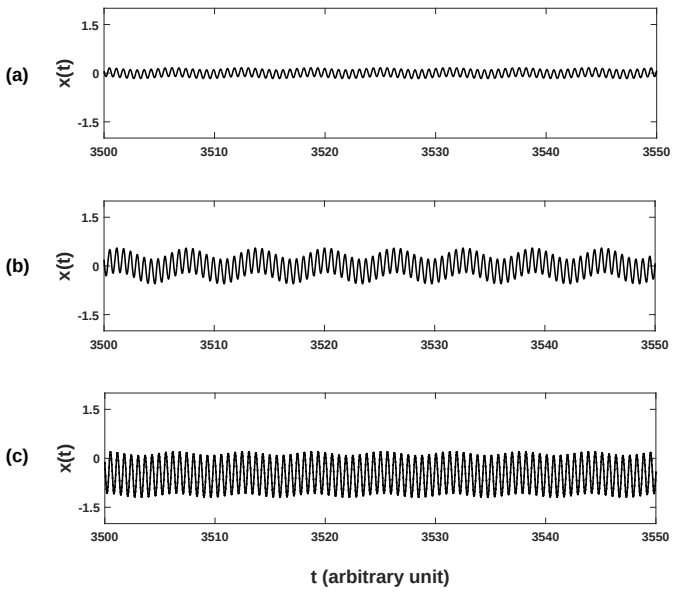

Figure 3: Typical time series of the Chua model experiencing the truncated sinusoidal force defined by eq. (4) and driven by the excitation of eq. (8). The chronograms of x have been obtained by increasing the perturbation amplitude starting from $B = 0$ with step $\Delta B = 0.01$ until (a) $B = 1.5$, (b) $B = 4.13$, (c) $B = 6.8$. Model parameters: $n = 1$, $k = 1$, $V_0 = \frac{\pi}{32}$, $\alpha = 6$, $\beta = 16$, $b = 0.1$, $\omega_1 = 1$, $\Omega = 10\omega_1$, numerical time step $\Delta t = 0.0015$.

3.2. Frequency analysis

By using Fourier transform, the output $x(t)$ of the system is analyzed with the corresponding unilateral magnitude spectrum defined by $2|X(f)|u(f)$. Here, $|X(f)|$ is the modulus of the Fourier transform and $u(f)$ is the Heaviside function. The unilateral magnitude spectrum is used to compute the linear response Q. Indeed, the linear response Q corresponds to the amplitude of the unilateral magnitude spectrum $2|X(f_1)|$ at the low frequency $f_1 = \frac{\omega_1}{2\pi}$ normalized by the amplitude b of the low frequency. The linear response Q formally writes as [2]:

$$Q = \frac{2|X(f_1)|}{b}. \tag{9}$$

The linear response Q, quantifies how the low frequency component is affected through the considered nonlinear

systems by the high frequency perturbation.

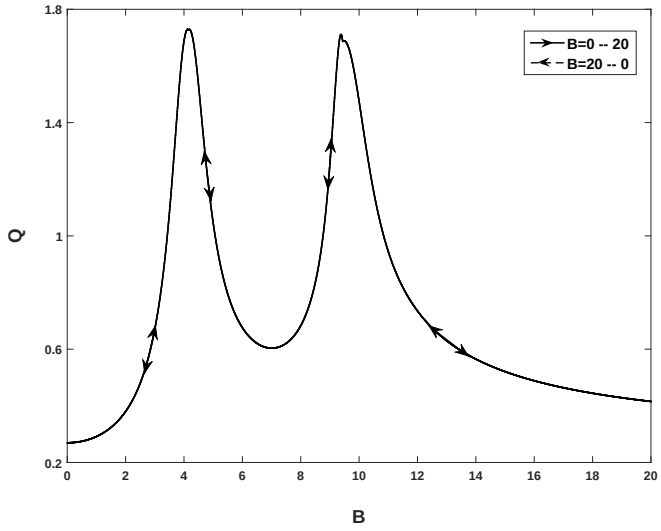

Figure 4: Linear response Q versus the perturbation amplitude B for a system experiencing the truncated sinusoidal force. The arrows indicate that increasing B from 0 to 20 or reducing B from 20 to 0 provide the same resonance curve. Parameters: $n = 1$, $k = 1$, $V_0 = \dfrac{\pi}{32}$, $\alpha = 6$, $\beta = 16$, $b = 0.1$, $\omega_1 = 1$, $\Omega = 10\omega_1$, perturbation amplitude step $\Delta B = 0.01$, numerical time step $\Delta t = 0.0015$.

Using the modus operandi given in Sec. 2.3, we integrate the system defined by the set of eq. (1), first with our truncated sinusoidal force defined by eq. (3) and secondly, with the sawtooth force expressed by eq. (4). The resonance curve of Fig. 4 depicts the evolution of the linear response Q versus the perturbation amplitude B for the case of the system experiencing the truncated sinusoidal force with nonlinearity order $n = 1$. Here, we vary the perturbation amplitude B, first in the "forward direction", that is from $B = 0$ to $B = 20$, and then return in the "reverse direction" from $B = 20$ to $B = 0$. The resonance curves corresponding to the forward and reverse directions, for the system experiencing the truncated sinusoidal force are superimposed, as shown at Fig. 4. The system then follows the same path in both directions and the resonance curves reveal two resonances which correspond to the number of unstable states in the system's potential well, that is $n + 1$. Increasing the perturbation amplitude B in the "forward direction", the first resonance gives the maximum response which decreases as the perturbation amplitude B keeps increasing.

In a similar way, considering the sawtooth nonlinearity with the order $n = 1$, we have obtained the resonance curves of Fig. 5, which were first reported in the work of K. Abirami et al [28]. Fig. 5 confirms their work with our notation for the sawtooth force expressed in eq. (3): varying the perturbation amplitude B in the forward and returning in reverse direction, the system follows two different paths near the peak of each resonance. In the forward direction, the last resonance provides the system's maximum response contrary to the case of the truncated sinusoidal force presented in Fig. 4.

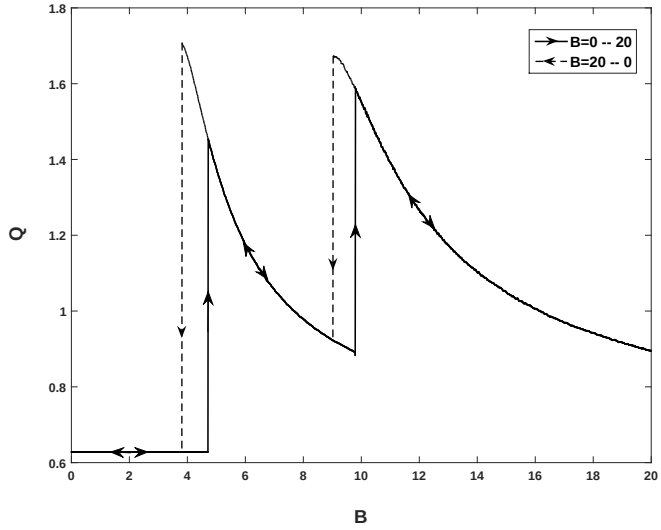

Figure 5: Linear response Q versus the perturbation amplitude B, for a system experiencing the sawtooth force. Our simulation results are in agreement with the one obtained by K. Abirami *et al* [28]. Parameters: $n = 1$, $A = 0.5$, $A_0 = 0.125$, $\alpha = 6$, $\beta = 16$, $b = 0.1$, $\omega_1 = 1$, $\Omega = 10\omega_1$, $\Delta B = 0.01$, $\Delta t = 0.0015$.

In comparison, the overall maximum response of our system with the truncated sinusoidal force in the forward direction is $Q^* = 1.729$, achieved for the optimal perturbation amplitude $B^* = 4.10$. This is better than the maximum response obtained with the sawtooth force in the forward direction, that is $Q^* = 1.587$ at $B^* = 9.81$. In effect, at Fig. 4, the system with our truncated sinusoidal force needs smaller perturbation amplitude $B^* = 4.10$ to reach

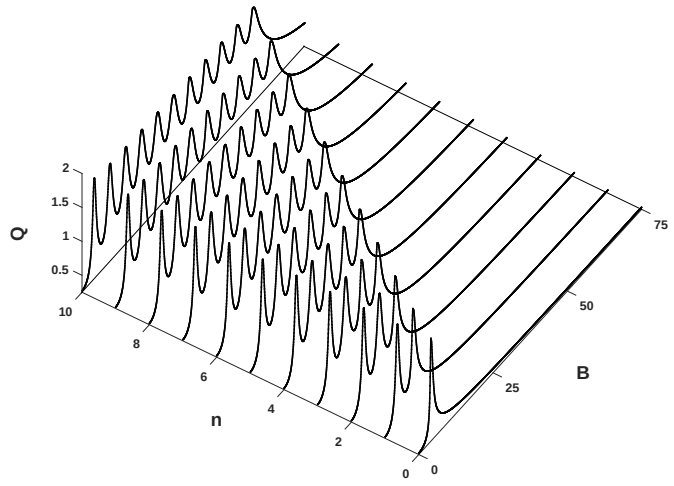

Figure 6: Overall resonance behavior of the system experiencing the truncated sinusoidal force in the perturbation amplitude B and nonlinearity order n parameters plane. The linear response Q is plotted versus B and n. Parameters: $k = 1$, $V_0 = \frac{\pi}{32}$, $\alpha = 6$, $\beta = 16$, $b = 0.1$, $\omega_1 = 1$, $\Omega = 10\omega_1$, $\Delta B = 0.01$, $\Delta t = 0.0015$.

its maximum response when compared to the system with the sawtooth force at Fig. 5 which requires $B^* = 9.81$. Moreover, increasing the perturbation amplitude B in the forward and returning in the reverse direction, our system follows the same path at Fig. 4. Note that hystereses at the breakpoints of each resonance are obtained only in the case of the system with the sawtooth force as represented in Fig. 5. The presence of these hystereses around the jumps may be due to the discontinuities which are observed at the unstable positions of the sawtooth force in Fig. 1 and which does not exist for the truncated sinusoidal force of Fig. 2.

The nonlinearity order n controls the number of resonances obtained for both nonlinearities. Fig. 6 provides the overall behavior of our system with the truncated sinusoidal force as a function of the nonlinearity order n. In fact, Fig. 6 shows that there are always $n + 1$ resonances which correspond to the number of unstable states set by the system's potential. For each value of n, the first resonance always provides the maximum response as depicted in Fig. 4 for $n = 1$. Indeed, afterwards the amplitude of the other observed resonances decrease. For the sake of clarity, we introduce $Q_m^{*,n}$ as the amplitude of the local maxima number m achieved by the linear response Q of a system with nonlinearity order n. Moreover, $B_m^{*,n}$ will refer to the amplitudes of the perturbation allowing to reach these local maxima $Q_m^{*,n}$.

To have another look of the general behavior of our system for each nonlinearity order n, we analyse the evolution of the local maxima $Q_m^{*,n}$ that the linear response Q reaches and which correspond to the response peak number m of Fig. 6. We therefore present in Figs. 7(a) – 7(d) the locus of the maximum response $Q_m^{*,n}$ at the resonance peaks of Fig. 6 for the nonlinearity order ranging from $n = 5$ to $n = 8$, versus the corresponding perturbation amplitude $B_m^{*,n}$ at which they occur. For instance, in the inset of Fig. 7(a), the linear response Q exhibits

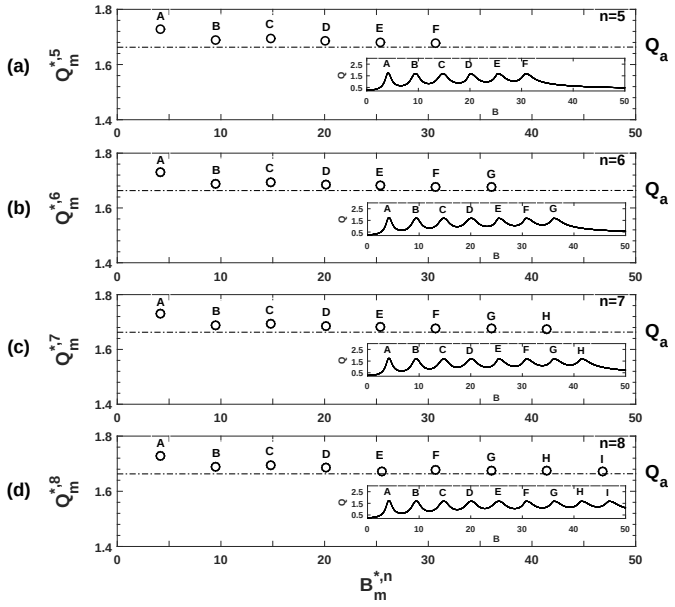

Figure 7: Locus of the linear response local maxima $Q_m^{*,n}$ versus the corresponding perturbation amplitude $B_m^{*,n}$ at which they occur. From top to bottom, we have considered a system experiencing a truncated sinusoidal force with order (a) $n = 5$, (b) $n = 6$, (c) $n = 7$ and (d) $n = 8$. The insets at each subfigure represent the classical linear response curves deduced from Fig. 6 where the maxima have been labeled with alphabetical capital letters. Parameters: $k = 1$, $V_0 = \frac{\pi}{32}$, $\alpha = 6$, $\beta = 16$, $b = 0.1$, $\omega_1 = 1$, $\Omega = 10\omega_1$, $\Delta B = 0.01$, $\Delta t = 0.0015$.

$m = 6$ resonances for the nonlinearity order $n = 5$. These resonances are referred by capital letters A, B, C, D, E and F. Therefore, we can see from Fig. 7(a), the locus of the local maxima $Q_m^{*,n}$ of each of these six resonances A, B, C, D, E and F versus the corresponding optimal perturbation amplitude $B_m^{*,n}$ at which they occur. Figs. 7(a) – 7(d) show that, whatever the nonlinearity order n, the first resonance is always the maximum response of our system after which, the magnitude of the m^{th} local maxima decreases as the nonlinearity order n increases. However, performing the same analyses on the system with the sawtooth force, Fig. 8 shows that the first resonance is always the minimum response. Moreover, the intensity of the maximum linear response $Q_m^{*,n}$ at the peak of the m^{th} local resonance increases as the nonlinearity order n increases.

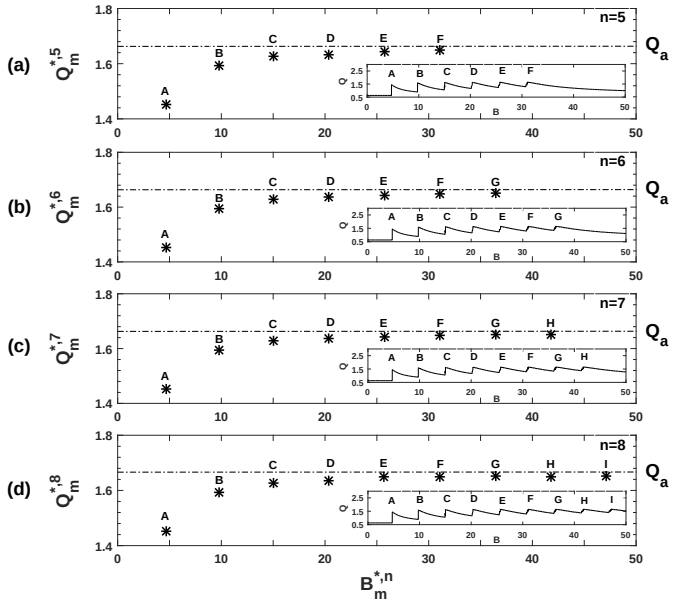

Figure 8: Locus of the linear response local maxima $Q_m^{*,n}$ versus the corresponding perturbation amplitude $B_m^{*,n}$ at which they occur. From top to bottom, we have considered a system experiencing a sawtooth force with order (a) $n = 5$, (b) $n = 6$, (c) $n = 7$ and (d) $n = 8$. The insets at each subfigure represent the classical linear response curves where the maxima have been labeled with alphabetical letters. Parameters: $A = 0.5$, $A_0 = 0.125$, $\alpha = 6$, $\beta = 16$, $b = 0.1$, $\omega_1 = 1$, $\Omega = 10\omega_1$, $\Delta B = 0.01$, $\Delta t = 0.0015$.

Note that, the maximum response $Q_m^{*,n}$ of the two systems from Figs. 7 and 8 tends to an asymptotic value Q_a as the nonlinearity order n keeps increasing. The asymptotic value of the two systems response, which is indicated with the dashed-line on both Fig. 7 and Fig. 8, is approximately $Q_a = 1.664$.

Therefore, it clearly appears that the advantage of the truncated sinusoidal nonlinearity is to provide the best response for the nonlinearity order $n = 0$, whereas to achieve the best resonance with the sawtooth force a greater nonlinearity order n must be considered.

The nonlinearity order n was shown to have directly controlled the number of resonances obtained in the two systems. However, we are now interested in exploring if n can enhance the system's local maximum linear response $Q_m^{*,n}$. We study the dependence of the two systems' local maximum responses $Q_m^{*,n}$ versus the nonlinearity order n, corresponding to the first, second, third and fourth maxima in Figs. 9(a), (b), (c) and (d) respectively. Circle-marked lines, which represent the response of the system with the truncated sinusoidal force are compared with the star-marked lines, which refer to the responses with the sawtooth force. As shown in all plots of Fig. 9, we understand that for each resonance, the maximum response $Q_m^{*,n}$ obtained in both the two systems does not significantly change due to the nonlinearity order n.

Furthermore, we can also understand from Fig. 9 that the responses of our system with the truncated sinusoidal force are more pronounced than those achieved with the sawtooth force. Lastly, as we are approaching the last maxima, the responses of the two systems tend to the asymptotic value Q_a, as indicated by the dashed-lines in all the plots of Fig. 9.

3.3. Analysis by phase portraits

In this part, we analyze the dynamical behavior of our system by means of phase portrait. In particular, we investigate the evolution of the resonance curve presented in Fig. 4, which corresponds to the response of

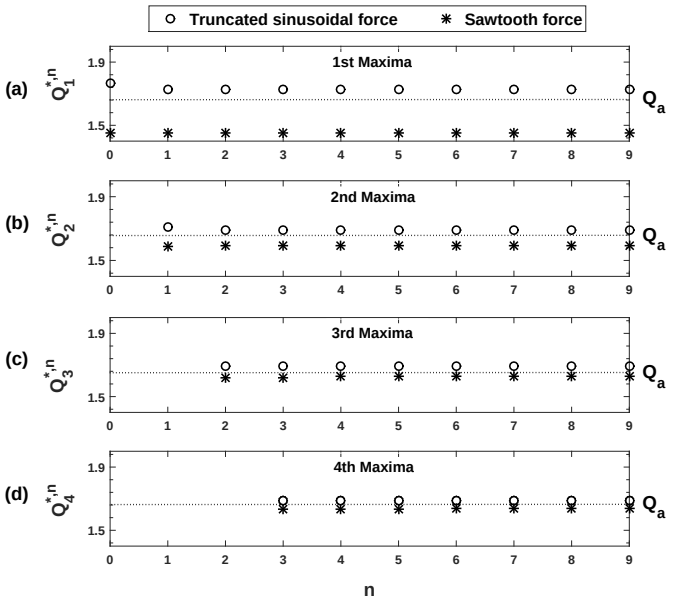

Figure 9: Evolution of each local maxima $Q_m^{*,n}$ reached by the linear response Q versus the nonlinearity order n. The performance obtained with the two nonlinear forces are compared when we consider: (a) The first maxima, (b) The second maxima, (c) The third maxima, (d) The fourth maxima. Circle-marked lines correspond to the truncated sinusoidal force whereas the star-marked lines refers to the sawtooth force. Parameters: $k = 1$, $V_0 = \frac{\pi}{32}$, $A = 0.5$, $A_0 = 0.125$, $\alpha = 6$, $\beta = 16$, $b = 0.1$, $\omega_1 = 1$, $\Omega = 10\omega_1$, $\Delta B = 0.01$, $\Delta t = 0.0015$.

our system with the truncated sinusoidal force for the order $n = 1$. For this nonlinearity order $n = 1$, the truncated sinusoidal force according to our notations, consists of three stable states located at positions $X^*_{-2,1} = -1$, $X^*_{0,1} = 0$, $X^*_{+2,1} = +1$ and two unstable states at positions $X^*_{-1,1} = -0.5$, $X^*_{+1,1} = +0.5$. We analyze the phase portraits behavior for six selected points on the resonance curve of Fig. 4. All simulations here start with the perturbation $B = 0$. The perturbation amplitude increases with step $\Delta B = 0.01$ and the last values of the system variables from the previous simulation are maintained as the initial conditions for the next simulation. Moreover, for each selected point on Fig. 4, we perform five different simulations, each of them with one of the stable and unstable positions as initial condition for x, and zero for the remaining variables. For example, to obtain the phase portrait for $B = 1.5$ at Fig. 10(a), we start with $B = 0$ and perform five different simulations each of them starting with one of the the initial conditions $x(0) = -1$, -0.5, 0, 0.5, 1 respectively, and $y(0) = z(0) = 0$. For each of these five simulations, the system exhibits at Fig. 10(a) periodic orbits which are centered on one of the stable or unstable positions of the system.

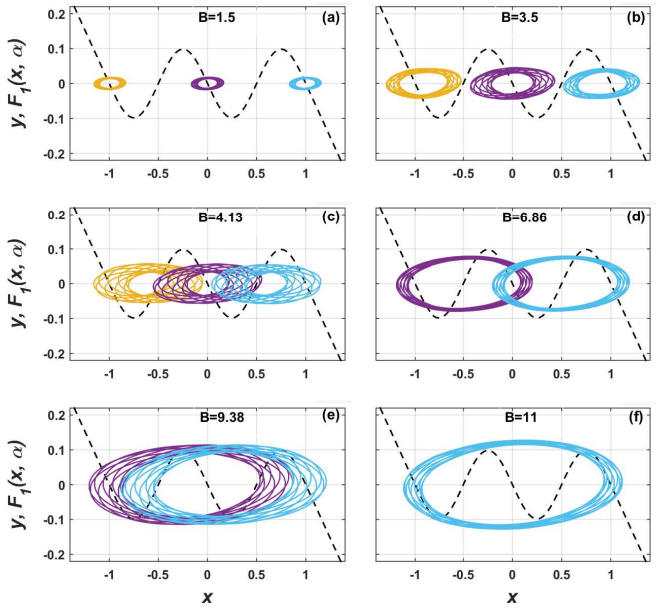

Figure 10: Phase portraits of the coexisting orbits for the resonance curve of Fig. 4. The perturbation amplitude is set to: (a) $B = 1.5$, (b) $B = 3.5$, (c) $B = 4.13$, (d) $B = 6.86$, (e) $B = 9.38$ and (f) $B = 11$. The equivalent truncated sinusoidal force $F_1(x, 1)$ is also superimposed using a dashed-line in all the cases. Parameters: $n = 1$, $k = 1$, $V_0 = \frac{\pi}{32}$, $\alpha = 6$, $\beta = 16$, $b = 0.1$, $\omega_1 = 1$, $\Omega = 10\omega_1$.

Therefore, setting the perturbation amplitude to $B = 1.5$ at Fig. 10(a) gives rise to periodic orbits centered around the three stable positions $X^*_{-2,1} = -1$, $X^*_{0,1} = 0$ and $X^*_{+2,1} = +1$. This implies that the orbits for the two unstable positions: $X^*_{-1,1} = -0.5$ and $X^*_{+1,1} = +0.5$ are attracted to the neighboring stable states. Increasing the perturbation amplitude to $B = 3.5$, the size of these periodic orbits increases, as shown at Fig. 10(b). At the peak of the first resonance of Fig. 4, which corresponds to $B = 4.13$, the size of these three orbits increase further and the two adjacent orbits overlap the middle orbit. However, increasing the perturbation amplitude B

beyond the peak of the first resonance, the linear response Q in Fig. 4 is decreasing. Consequently, we obtain two periodic orbits centered around the two unstable points. These orbits overlap at the bottom of the first resonance, that is when $B = 6.86$, as presented in Fig. 10(d). The size of these two orbits keeps increasing as the perturbation amplitude B increases until at the peak of the second resonance when $B = 9.38$, the orbits coincide with each other as shown in Fig. 10(e). Lastly, for perturbation amplitude beyond the second resonance of Fig. 4, there will be no other resonance. This leads to the birth of one periodic orbit centered about the stable point at $X^*_{0,1} = 0$. The size of this orbit increases as the perturbation amplitude increases, as depicted for $B = 11$ in Fig. 10(f). The phase portrait analysis presented in Fig. 10 illustrates that our system with the truncated sinusoidal force exhibits resonance effect, depending on the perturbation amplitude B. We identify the observed resonance effect as VR phenomenon which was also observed with the system experiencing a sawtooth force by K. Abirami *et al* [28].

4. Ghost-vibrational resonance

In this section, we consider that the system is driven by two signals with close low angular frequencies ω_1 and ω_2, corrupted by a high frequency perturbation of amplitude B and angular frequency Ω. The boolean variable δ in eq. (6) is then taken as $\delta = 1$ such that, the input perturbed excitation $e_p(t)$ defined in Sec. 2.2 by eq. (5) reduces to

$$e_p(t) = b\Big[\cos(\omega_1 t) + \cos(\omega_2 t)\Big] + B\cos\Omega t. \qquad (10)$$

Especially, the gap ω_0 between the two input angular frequencies, $\omega_1 = 2\omega_0$ and $\omega_2 = 3\omega_0$ is fixed to $\omega_0 = 0.1$ which constitutes the system's ghost angular frequency. Moreover, the amplitude of the low frequencies is set to $b = 0.04$ while the perturbation angular frequency is tuned to $\Omega = 20\omega_0$. Lastly, we take the parameter values $\alpha = 4$ and $\beta = 14$ for our system described by eq. 1.

By using the simulation algorithm precised in Sec. 2.3, we integrate the system given by eqs. (1) with the truncated sinusoidal force $F_n(x, \alpha)$ and the input perturbed excitation $e_p(t)$ defined by eqs. (4) and (10) respectively. This section is devoted to the analysis of the system's response at the missing low angular frequency ω_0 but also at the two input low angular frequencies ω_1, and ω_2.

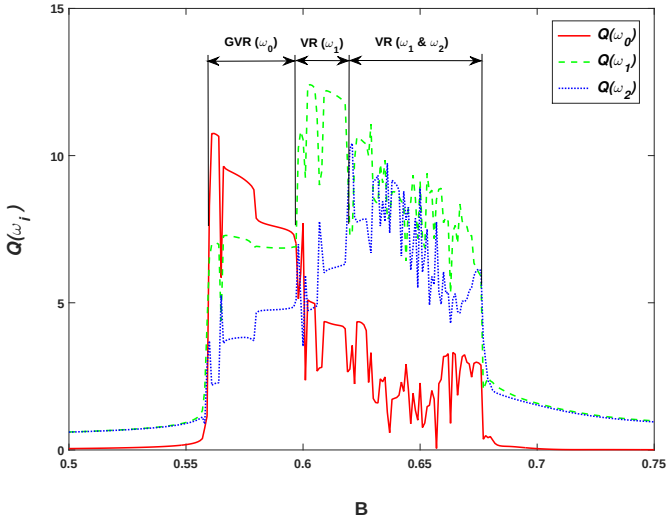

Figure 11: Linear response of the system Q at the low angular frequencies ω_0, ω_1 and ω_2, versus the perturbation amplitude B, for the system experiencing the truncated sinusoidal force. Parameters: $n = 0$, $k = 1$, $V_0 = \frac{\pi}{32}$, $\alpha = 4$, $\beta = 14$, $b = 0.04$, $\omega_0 = 0.1$, $\omega_1 = 2\omega_0$, $\omega_2 = 3\omega_0$, $\Omega = 20\omega_0$, $\Delta B = 0.001$, $\Delta t = 0.0015$.

Results presented in Fig. 11 show the linear responses $Q(\omega_0)$, $Q(\omega_1)$ and $Q(\omega_2)$ of the system at the missing low angular frequency ω_0 and at the two input low angular frequencies (ω_1 and ω_2), versus the perturbation amplitude B. Without perturbation, namely $B = 0$, the system's linear response $Q(\omega_0)$ at the missing low angular frequency ω_0 is null, contrary to the linear responses $Q(\omega_1)$ and $Q(\omega_2)$ at the two input low angular frequencies. However, as the perturbation amplitude B increases, the system reveals resonances at the missing low angular frequency ω_0 and at the two input low angular frequencies (ω_1 and ω_2) whose predominance can be identified within different ranges of the perturbation B. In the first resonance region, where the perturbation amplitude B is

in the range $[0.560; 0.597]$, we observe an enhancement of the system's linear response $Q(\omega_i)$ at the three angular frequencies ω_0, ω_1 and ω_2. Moreover, the linear response $Q(\omega_0)$ at the missing angular frequency ω_0 is the predominant one. However, for the perturbation amplitude B in the interval $[0.598; 0.619]$, the system's linear response $Q(\omega_1)$ at the input low angular frequency ω_1 becomes predominant. Similarly, for the perturbation amplitude B in the interval $[0.620; 0.676]$, the linear response of the system at the two low angular frequencies ω_1 and ω_2 interchangeably dominate but each in a short interval of B. Lastly, as the perturbation amplitude B keeps increasing beyond $B = 0.676$, the system's linear response $Q(\omega_0)$ at the missing angular frequency ω_0 approaches zero whereas the responses $Q(\omega_1)$ and $Q(\omega_2)$ at the two low angular frequencies ω_1 and ω_2 are amplified in the same way, none of the two being predominant.

To better understand the evolution of the resonances observed in Fig. 11, chronograms and their corresponding spectra are respectively presented at Fig. 12(a) - (d) and Fig. 13(a) - (d), for four specific values of the perturbation amplitude B, namely 0.561, 0.603, 0.621 and 0.629. We first choose the value $B = 0.561$ to show the predominance of GVR at the ghost angular frequency ω_0 in the first resonance region of Fig. 11 defined by the range of the perturbation amplitude $[0.560; 0.597]$. Next, the value $B = 0.603$ allows to observe the superiority of VR effect at the angular frequency ω_1 in the second resonance region of Fig. 11 defined by the perturbation range $[0.598; 0.619]$. Lastly, considering $B = 0.621$ and $B = 0.629$ allow to illustrate the predominance of VR at the angular frequencies ω_2 and ω_1 in the last resonance region of Fig. 11 where B is in the range $[0.620; 0.676]$. Note that to visualize at which frequency the system synchronizes its response, we have superimposed the corresponding predominant low frequency sinusoidal wave in each chronogram of Fig. 12. Additionally, for all the spectra of Fig. 13, we have labeled the value of unilateral magnitude spectrum $2|X(f_i)|$ corresponding to each low frequency, namely $f_0 = \dfrac{\omega_0}{2\pi}$, $f_1 = \dfrac{\omega_1}{2\pi}$ and $f_2 = \dfrac{\omega_2}{2\pi}$.

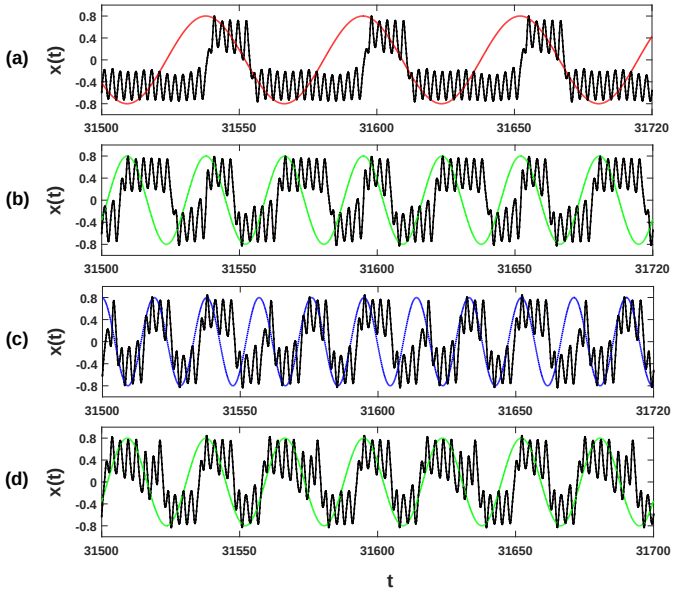

Figure 12: Chronograms summarizing the system's behavior for four specific values of the perturbation amplitude B taken in the different ranges identified at Fig. 11. The system synchronizes its response to the sinusoidal wave superimposed on each subfigure and which corresponds to the predominant angular frequency, that is, ω_0, ω_1, ω_2 and ω_1 for subfigures (a), (b), (c) and (d) respectively. From top to bottom, we observe the predominance of: (a) GVR at the ghost angular frequency ω_0 when $B = 0.561$ (first resonance region of Fig. 11), (b) VR at the angular frequency ω_1 when $B = 0.603$ (second resonance region of Fig. 11), (c) VR at the angular frequency ω_2 when $B = 0.621$ (third resonance region of Fig. 11) and (d) VR at the angular frequency ω_1 when $B = 0.629$ (third resonance region of Fig. 11). Parameters: $n = 0$, $k = 1$, $V_0 = \dfrac{\pi}{32}$, $\alpha = 4$, $\beta = 14$, $b = 0.04$, $\omega_0 = 0.1$, $\omega_1 = 2\omega_0$, $\omega_2 = 3\omega_0$, $\Omega = 20\omega_0$, $B = 0.561$, $\Delta t = 0.0015$.

In the first resonance region of Fig. 11 where GVR effect is predominant, that is for $B \in [0.560; 0.597]$, Fig. 12(a) shows that the enclosed signal at the ghost angular frequency ω_0 synchronizes with the slow oscillations of the time series. In addition, the corresponding unilateral magnitude spectrum at Fig. 13(a) also confirms that the amplitude of the spectrum $2|X(f_0)|$ at the ghost angular frequency ω_0 is best pronounced in this particular region.

By contrast, the system's temporal response of Fig. 12(b) and its corresponding spectrum of Fig. 13(b) have

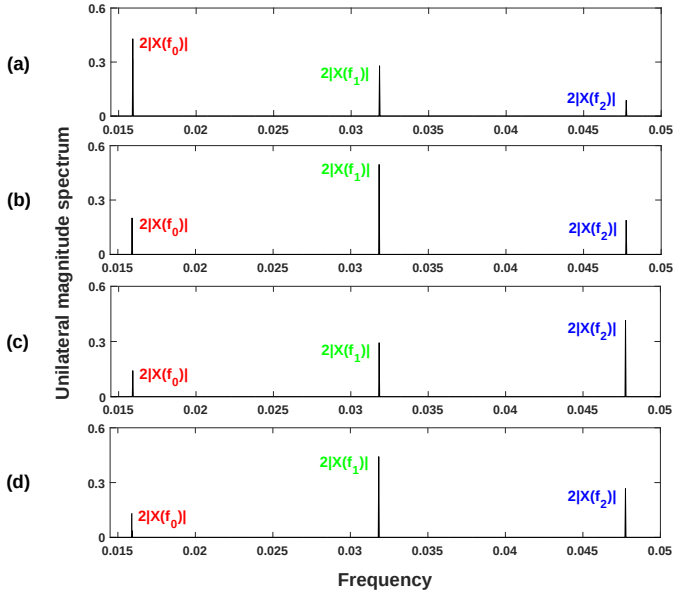

Figure 13: Unilateral magnitude spectra of the time series of Fig. 12. The spectral responses clearly indicate which frequency is dominant in each case. Parameters: $n = 0$, $k = 1$, $V_0 = \frac{\pi}{32}$, $\alpha = 4$, $\beta = 14$, $b = 0.04$, $\omega_0 = 0.1$, $\omega_1 = 2\omega_0$, $\omega_2 = 3\omega_0$, $\Omega = 20\omega_0$, $B = 0.561$, $\Delta t = 0.0015$.

been obtained for the perturbation amplitude from the second resonance region, where VR effect at the angular frequency ω_1 is the best pronounced resonance. In this resonance region, for which the perturbation amplitude B is in the range $[0.598; 0.619]$, the chronogram of Fig. 12(b) shows that the slow oscillations of the temporal response are in phase with the superimposed sinusoidal wave at the angular frequency ω_1. Moreover, the corresponding spectra at Fig. 13(b) confirms that the response of the system at the angular frequency ω_1 is the predominant one.

In the last resonance region of Fig. 11 defined by the range of perturbation amplitude $[0.620; 0.676]$, the chronograms of Figs. 12(c) and 12(d) with their corresponding spectra at Figs. 13(c) and 13(d) show that VR at the angular frequencies ω_2 and ω_1 interchangeably emerge as the best pronounced resonances. The chronogram of Fig. 12(c), obtained for $B = 0.621$, illustrates the predominance of VR at the angular frequency ω_2, since the slow oscillations of the temporal response synchronizes with the superimposed sinusoidal wave at the angular frequency ω_2. Furthermore, the corresponding spectrum at Fig. 13(c) proves that the system's response at the angular frequency ω_2 is the best pronounced one. Similarly, the time series of Fig. 12(d) and its corresponding spectrum at Fig. 13(d), obtained for $B = 0.629$, refer to the predominance of VR effect at the angular frequency ω_1.

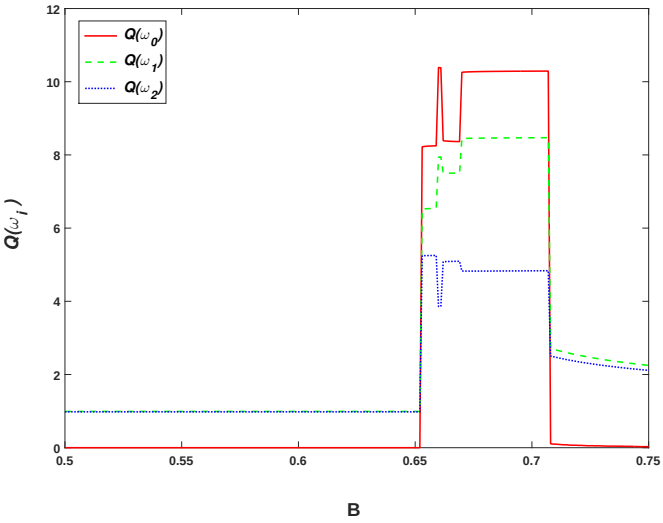

Figure 14: Linear response Q of the system at the angular frequencies ω_0, ω_1 and ω_2 versus the perturbation amplitude B, for the system experiencing the sawtooth force. Parameters: $n = 0$, $A = 0.5$, $A_0 = 0.125$, $\alpha = 4$, $\beta = 14$, $b = 0.04$, $\omega_0 = 0.1$, $\omega_1 = 2\omega_0$, $\omega_2 = 3\omega_0$, $\Omega = 20\omega_0$, $\Delta B = 0.001$, $\Delta t = 0.0015$.

These resonance behaviors of the system submitted to the truncated sinusoidal force were not obtained in the case of the system experiencing a sawtooth force, for the considered parameter settings. Indeed, our simulation of the system with the sawtooth force reported at Fig. 14, confirms the behavior observed by K. Abirami *et al* [28]: varying the perturbation amplitude B induces all the resonance effects in the same perturbation range $[0.652; 0.708]$, with the linear response $Q(\omega_0)$ at the ghost angular frequency ω_0 predominant in the whole region. Note that, the system experiencing the sawtooth force can also exhibits the behavior which has been reported at Fig. 11 in the case of the truncated sinusoidal force. However, in this regard, it is necessary to change the system parameters such as the nonlinearity order n, the low frequencies

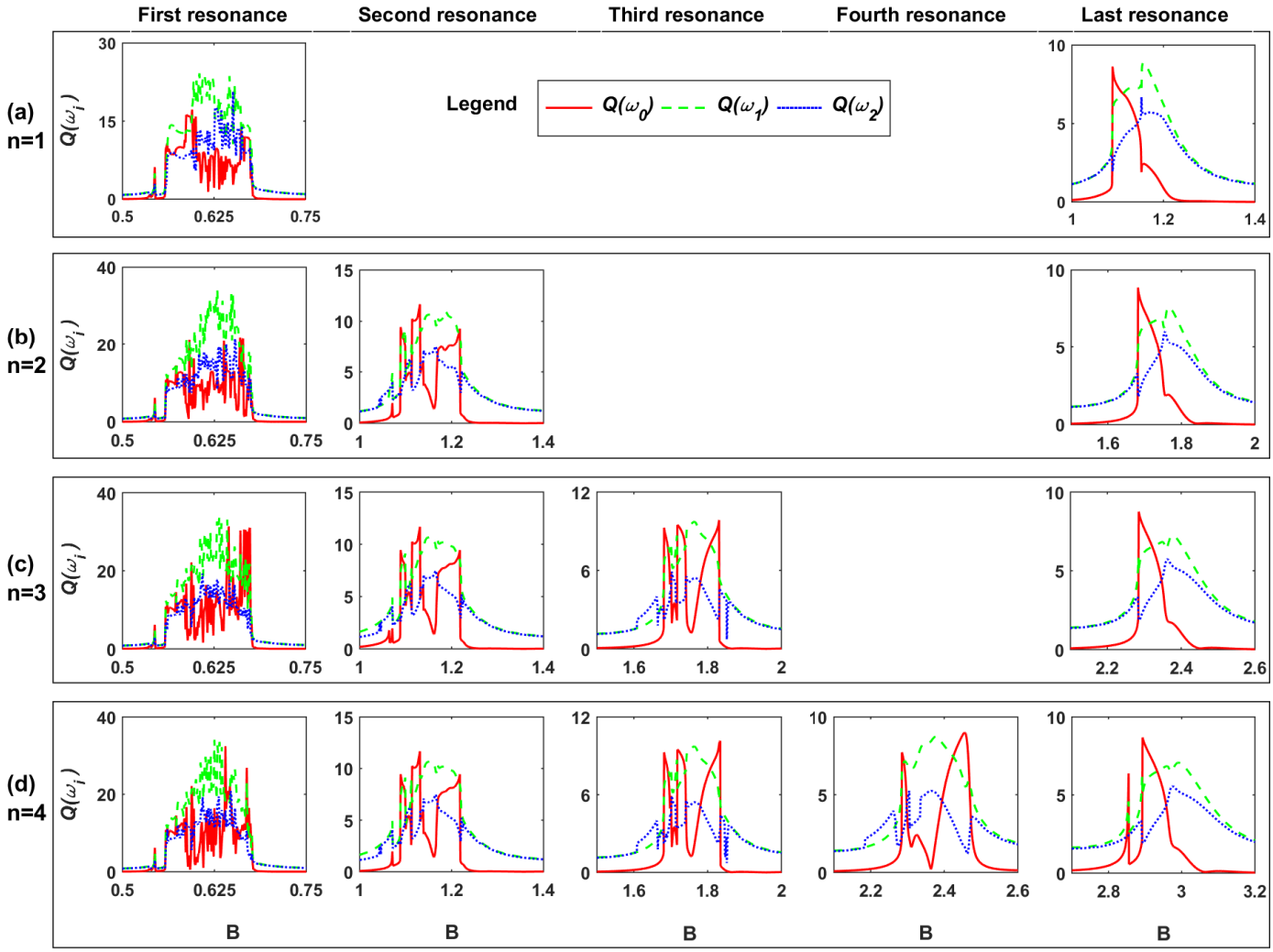

Figure 15: Impact of the nonlinearity order n of the truncated sinusoidal force on the resonances. The linear response Q estimated at the angular frequencies ω_0, ω_1 and ω_2 has been plotted versus the perturbation amplitude B, for the nonlinearity orders: (a) $n = 1$, (b) $n = 2$, (c) $n = 3$, (d) $n = 4$. Parameters: $k = 1$, $V_0 = \frac{\pi}{32}$, $\alpha = 4$, $\beta = 14$, $b = 0.04$, $\omega_0 = 0.1$, $\omega_1 = 2\omega_0$, $\omega_2 = 3\omega_0$, $\Omega = 20\omega_0$, $\Delta B = 0.01$, $\Delta t = 0.0015$.

amplitude b and the perturbation angular frequency Ω.

Concerning the system with the truncated sinusoidal force, the separation of the different resonance effects in distinct ranges of perturbation amplitude B, is not restricted to the nonlinearity order $n = 0$. Indeed, for the nonlinearity orders n presented at Fig. 15, namely 1, 2, 3 and 4, our system also follows the same behavior as achieved at Fig. 11 for $n = 0$. For each considered nonlinearity order n, we obtained $n + 1$ resonances which have been plotted separately at Fig. 15 with an appropriate zoom near each resonance. Interestingly, we observed the same trend for each resonance, whatever the nonlinearity order n.

5. Conclusion

In this paper, we have considered the dynamics of a modified Chua's circuit model, experiencing a truncated sinusoidal force and driven by a perturbed input excitation: low frequency signals corrupted by a high frequency perturbation. In particular, we studied the impact of the system's nonlinearity on the occurrence of Vibrational Resonance (VR) and Ghost-Vibrational Resonance (GVR) phenomena. In the previous work of K. Abirami et al devoted to this Chua system, VR and GVR were studied by con-

sidering a sawtooth nonlinearity [28]. In the present work, we analyzed the impact of the system's nonlinearity on the occurrence of VR and GVR, since we compared the system responses obtained with the truncated sinusoidal force and those with the sawtooth force. Consequently, the same potential barrier height and periodicity were considered in both systems.

Our VR studies with the truncated sinusoidal force revealed multiple resonances whose intensity reduces as the perturbation amplitude B increases. As initially reported by K. Abirami et al [28], our simulations with the sawtooth force also revealed multiple resonances. However, in this latter case, we have established that the intensity of the first resonance is the weakest one. More precisely, contrary to the truncated sinusoidal force, the intensity of the local maxima increases with the perturbation amplitude B. We have also shown that the number of resonances obtained with both nonlinearities is controlled by their order n which also represents the number of unstable states in the system.

It is interesting to remark that, our system with the truncated sinusoidal force requires smaller perturbation amplitude B to reach its maximum response. Consequently, it is less energy consuming when compared to the system experiencing a sawtooth force, which requires relatively larger perturbation amplitude B to attain its maximum response. In addition, as the nonlinearity order n in both the two systems keeps increasing, the response of the two systems approaches an asymptotic value Q_a which for our parameters setting has been estimated to $Q_a = 1.664$.

Next, in the case of the truncated sinusoidal force, we have interpreted the multiple resonances observed by means of phase portraits analyses. For a weak value of the perturbation amplitude B, our system revealed orbits with small amplitudes, each of them being centered around one of the stable positions of the system's potential. When the perturbation B increases, the enhancement of the system's linear response Q is manifested in an enlargement of the existing orbits. At the peak of each resonance, the existing adjacent orbits overlap with each other. However, increasing the perturbation amplitude B beyond the peak of each resonance, one of the existing orbits disappeared. After the peak of the last resonance, the system revealed just one orbit whose size grows with the increase of the perturbation amplitude B.

Exciting the system experiencing the truncated sinusoidal nonlinearity with two close low frequency signals, we have established that a high frequency perturbation can induce resonances at the two input low angular frequencies ω_1 and ω_2, together with another resonance at a missing input low angular frequency ω_0. The predominance of each of these resonances can be identified in a specific range of the perturbation amplitude B. In the first range of the perturbation amplitude, the system's response at the missing low angular frequency ω_0 emerges as the best pronounced resonance which indicates a strong manifestation of GVR effect. Another resonance region is defined by a second range of the perturbation amplitude B where the system's linear response at the low angular frequency ω_1 is the strongest. It corresponds to the occurrence of VR effect at the angular frequency ω_1. In the last region, obtained for a third range of perturbation amplitude B, VR effects at the low angular frequencies ω_2 and ω_1 interchangeably become the dominant resonances. Our temporal analyses also confirmed which resonance is the most pronounced one since it has revealed that the system can synchronize its response with the ghost frequency or one of the two input low frequencies. In fact, it depends on which of the previously established ranges the perturbation amplitude B is taken. By contrast, for the system experiencing the sawtooth force, all the observed resonance effects occurred in only one specific range of the perturbation amplitude B, with the GVR as the predominant resonance throughout.

As we have shown that Chua circuit model with the truncated sinusoidal nonlinearity provides a better response

than with the sawtooth nonlinearity, we suspect that considering such nonlinearity might lead to interesting applications in engineering fields. Lastly, we trust that the nonlinearity presented in this paper, owing to its multistable behaviour, offers the opportunity to study the existence of multiscrolls as observed in the same Chua model but with a sawtooth multistable function.

References

[1] L. Gammaitoni, P. Hänggi, P. Jung, F. Marchesoni, Stochastic resonance: a remarkable idea that changed our perception of noise, Eur. Phys. J. B 69 (2009) 1–3.

[2] P. S. Landa, P. V. E. McClintock, Vibrational resonance, J. Phys. A 33 (2000) L433.

[3] F. Chapeau-Blondeau, X. Godivier, N. Chambet, Stochastic resonance in a neuron model that transmits spike trains, Phys. Rev. E 53 (1996) 1273.

[4] D. Nozaki, Y. Yamamoto, Enhancement of stochastic resonance in a fitzhugh-nagumo neuronal model driven by colored noise, Phys. Lett. A 243 (1998) 281–287.

[5] D. G. Luchinsky, R. Mannella, P. V. E. McClintock, N. G. Stocks, Stochastic resonance in electrical circuits - I: Conventional stochastic resonance, IEEE Trans. on Circuits and Syst. - II 46 (1999) 1205–1214.

[6] E. Ullner, A. Zaikin, J. García-Ojalvo, R. Bascones, J. Kurths, Vibrational resonance and vibrational propagation in excitable systems, Phys. Lett. A 312 (2003) 348–354.

[7] V. N. Chizhevsky, E. Smeu, G. Giacomelli, Experimental evidence of "vibrational resonance" in an optical system, Phys. Rev. Lett. 91 (2003) 220602.

[8] M. Bordet, S. Morfu, Experimental and numerical enhancement of vibrational resonance in neural circuit, Electron. Lett. 48 (2012) 903–905.

[9] M. Bordet, S. Morfu, Experimental and numerical study of noise effects in a FitzHugh–Nagumo system driven by a biharmonic signal, Chaos Solitons Fractals. 54 (2013) 82–89.

[10] T. O. Roy-Layinde, J. A. Laoye, O. O. Popoola, U. E. Vincent, Analysis of vibrational resonance in bi-harmonically driven plasma, Chaos 26 (2016) 093117.

[11] S. Morfu, M. Bordet, On the propagation of a low frequency excitation in a perturbed FitzHugh–Nagumo system: Simulation and experiments, Chaos Solitons Fractals. 103 (2017) 205–212.

[12] S. Morfu, M. Bordet, On the correlation between phase-locking modes and vibrational resonance in a neuronal model, Commun Nonlinear Sci. Numer. Simul. 55 (2018) 277–286.

[13] B. I. Usama, S. Morfu, P. Marquié, Numerical analyses of the vibrational resonance occurrence in a nonlinear dissipative system, Chaos Solitons Fractals. 127 (2019) 31–37.

[14] R. Gui, Y. Wang, Y. Yao, G. Cheng, Enhanced logical vibrational resonance in a two-well potential system, Chaos Solitons Fractals. 138 (2020) 109952.

[15] F. Duan, D. Abbott, Binary modulated signal detection in a bistable receiver with stochastic resonance, Physica A 376 (2007) 173–190.

[16] F. Duan, F. Chapeau-Blondeau, D. Abbott, Weak signal detection: condition for noise induced enhancement, Dig. Sig. Proc. 23 (2013) 1585–1591.

[17] Y. Ren, Y. Pan, F. Duan, F. Chapeau-Blondeau, D. Abbott, Exploiting vibrational resonance in weak-signal detection, Phys. Rev. E 96 (2017) 022141.

[18] Y. Ren, Y. Pan, F. Duan, Generalized energy detector for weak random signals via vibrational resonance, Phys. Lett. A 382 (2018) 806–810.

[19] L. Ning, Z. Chen, Vibrational resonance analysis in a gene transcriptional regulatory system with two different forms of time-delays, Physica D 401 (2020) 132164.

[20] E. Simonotto, M. Riani, C. Seife, M. Roberts, J. Twitty, F. Moss, Visual perception of stochastic resonance, Phys. Rev. lett 78 (1997) 1186.

[21] T. Aihara, K. Kitajo, D. Nozaki, Y. Yamamoto, Internal noise determines external stochastic resonance in visual perception, Vision research 48 (2008) 1569–1573.

[22] S. Morfu, B. I. Usama, P. Marquié, Perception enhancement of subthreshold noisy image with vibrational resonance, Electron. Lett. 55 (2019) 650–652.

[23] S. Morfu, B. I. Usama, P. Marquié, On some applications of vibrational resonance on image perception: The role of the perturbation parameters, Phil. Trans. R. Soc. A 379 (2021) 20200240.

[24] O. Calvo, D. R. Chialvo, Ghost stochastic resonance in an electronic circuit, Int. J. Bifurc. Chaos 16 (2006) 731–735.

[25] P. Balenzuela, H. Braun, D. R. Chialvo, The ghost of stochastic resonance: an introductory review, Contemp. Phys. 53 (2012) 17–38.

[26] M. Bordet, S. Morfu, P. Marquié, Ghost stochastic resonance in FitzHugh–Nagumo circuit, Electron. lett. 50 (2014) 861–862.

[27] M. Bordet, S. Morfu, P. Marquié, Ghost responses of the FitzHugh–Nagumo system induced by colored noise, Chaos Solitons Fractals. 78 (2015) 205–214.

[28] K. Abirami, S. Rajasekar, M. A. Sanjuán, Vibrational and ghost-vibrational resonances in a modified Chua's circuit model equation, Int. J. Bifurc. Chaos 24 (2014) 1430031.

[29] S. Rajamani, S. Rajasekar, M. A. F. Sanjuán, Ghost-vibrational resonance, Commun. Nonlinear Sc. Numer. Simulat. 19 (2014)

4003–4012.

[30] S. Morfu, B. Nofiele, P. Marquié, On the use of multistability for image processing, Phys. Lett. A 367 (2007) 192–198.

[31] L. O. Chua, The genesis of Chua's circuit, Electronics Research Laboratory, College of Engineering, University of California, 1992.

[32] J. A. Suykens, J. Vandewalle, Generation of n-double scrolls (n= 1, 2, 3, 4,...), IEEE Trans. on Circuits and Syst. - I 40 (1993) 861–867.

[33] S. Yu, W. K. Tang, G. Chen, Generation of n× m-scroll attractors under a chua-circuit framework, Chaos 17 (2007) 3951–3964.

[34] A. I. Khibnik, D. Roose, L. O. Chua, On periodic orbits and homoclinic bifurcations in chua's circuit with a smooth nonlinearity, Int. J. Bifurc. Chaos 3 (1993) 363–384.

[35] J. Yang, L. Zhao, Bifurcation analysis and chaos control of the modified chua's circuit system, Chaos Solitons Fractals. 77 (2015) 332–339.

[36] S. Arathi, S. Rajasekar, J. Kurths, Stochastic and coherence resonances in a modified Chua's circuit system with multi-scroll orbits, Int. J. Bifurc. Chaos 23 (2013) 1350132.

[37] R. Jothimurugan, K. Thamilmaran, S. Rajasekar, M. A. F. Sanjuán, Experimental evidence for vibrational resonance and enhanced signal transmission in Chua's circuit, Int. J. Bifurc. Chaos 23 (2013) 1350189.

[38] A. G. Radwan, M. A. Zidan, K. N. Salama, HP memristor mathematical model for periodic signals and dc, in: 2010 53rd IEEE International Midwest Symposium on Circuits and Systems, IEEE, 2010, pp. 861–864.

[39] C. Yakopcic, T. M. Taha, G. Subramanyam, R. E. Pino, S. Rogers, A memristor device model, IEEE Electron Device Lett. 32 (2011) 1436–1438.

[40] H. Kim, M. P. Sah, C. Yang, S. Cho, L. O. Chua, Memristor emulator for memristor circuit applications, IEEE Transactions on Circuits and Systems I: Regular Papers 59 (2012) 2422–2431.

[41] T. Matsumoto, A chaotic attractor from Chua's circuit, IEEE Trans. on Circuits and Syst. 31 (1984) 1055–1058.

[42] G.-Q. Zhong, F. Ayrom, Experimental confirmation of chaos from Chua's circuit, Int. J. Circuit Theory Appl. 13 (1985) 93–98.

[43] A. I. Mahla, Á. G. Badan Palhares, Chua's circuit with a discontinuous nonlinearity, J. Circuit. Syst. Comp. 3 (1993) 231–237.

[44] M. A. Aziz-Alaoui, Differential equations with multispiral attractors, Int. J. Bifurc. Chaos 9 (1999) 1009–1039.

[45] C.-H. Lamarque, O. Janin, J. Awrejcewicz, Chua systems with discontinuities, Int. J. Bifurc. Chaos 9 (1999) 591–616.

[46] J. Lu, G. Chen, X. Yu, H. Leung, Design and analysis of multiscroll chaotic attractors from saturated function series, IEEE Trans. on Circuits and Syst. - I 51 (2004) 2476–2490.